

Mapping Drug-Induced Neuropathy through In-Situ Motor Protein Tracking and Machine Learning

Zhigao Yi, Huxin Gao, Xianglin Ji, Xin-Yi Yeo, Suet Yen Chong, Yujie Mao, Baiwen Luo, Chao Shen, Sanyang Han, Jiong-Wei Wang, Sangyong Jung, Peng Shi, Hongliang Ren, and Xiaogang Liu*

Cite This: *J. Am. Chem. Soc.* 2021, 143, 14907–14915

Read Online

ACCESS |



Metrics & More

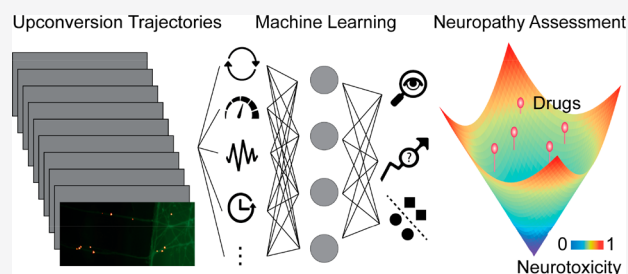


Article Recommendations



Supporting Information

ABSTRACT: Chemotherapy can induce toxicity in the central and peripheral nervous systems and result in chronic adverse reactions that impede continuous treatment and reduce patient quality of life. There is a current lack of research to predict, identify, and offset drug-induced neurotoxicity. Rapid and accurate assessment of potential neuropathy is crucial for cost-effective diagnosis and treatment. Here we report dynamic near-infrared upconversion imaging that allows intraneuronal transport to be traced in real time with millisecond resolution, but without photobleaching or blinking. Drug-induced neurotoxicity can be screened prior to phenotyping, on the basis of subtle abnormalities of kinetic characteristics in intraneuronal transport. Moreover, we demonstrate that combining the upconverting nanoplatform with machine learning offers a powerful tool for mapping chemotherapy-induced peripheral neuropathy and assessing drug-induced neurotoxicity.



INTRODUCTION

Chemotherapy-induced peripheral neuropathy (CIPN) is a common complication of antineoplastic therapy, characterized by symptoms such as pain, numbness, slow response, and impaired sensation that could lead to premature termination of patient treatment.^{1–6} A reliable and robust diagnostic strategy to CIPN is pending and is urgent to exploit because current clinical practices mainly rely on subjective and imprecise self-reporting from patients. CIPN is usually associated with impairment of intraneuronal transport, which regulates critical physiological activities such as signal transduction and transport of nutrients and organelles in neurons.^{7–12} Dynamic tracking with fluorescence microscopy would be suitable for quantification of subtle changes in intraneuronal cargo movement and therefore contribute to CIPN diagnosis. However, it has been challenging to maintain a high fidelity of intraneuronal trajectories and establish a standard protocol for neurotoxicity assessment.

Previous attempts to quantify cargo transport dynamics have been limited by low-fidelity recording due to the inherent constraints of conventional fluorescent probes such as molecular dyes, fluorescent proteins, quantum dots, and nanodiamonds (Figure 1a and Table S1).^{13–20} Although molecular fluorophore-labeled organelles enable movement tracking, low-contrast imaging due to photobleaching and autofluorescence typically occurs.^{13,14} The genetic transfection of fluorescent proteins is often limited by low transfection efficiency, uncontrolled overproduction of proteins, and severe photobleaching.^{15,16} Quantum dots feature high photolumi-

nescence efficiency and photostability but are plagued by photoblinking and cytotoxicity.^{17,18} Lanthanide-activated upconversion nanoparticles have shown promise as alternative bioprobes for cell imaging, neuromodulation, and other biomedical applications due to their excellent photostability and nonblinking characteristics.^{21–29} Our previous study has demonstrated the feasibility of intraneuronal tracking in multi-layer neuron cultures using upconversion nanoparticles.²¹ However, the low-fidelity tracking at 7 Hz is unlikely to distinguish CIPN, especially before phenotyping. It is thus essential to improve the readout at a single-nanoparticle level to achieve high-fidelity recording of intraneuronal movements. Moreover, data processing and learning are of significance in correlations between intraneuronal movements and neurotoxicity. The deployment of artificial intelligence in photonics has yielded transformative advances in data-driven optics, neural networks, and brain–computer interfacing.^{30–32} Artificial intelligence, such as machine learning, would be an irreplaceable technique to identify and quantify high-fidelity intraneuronal tracking among an enormous amount of data (Figure 1b). We reasoned that a powerful platform for mapping drug-induced neuropathy would be established with

Received: July 14, 2021

Published: September 1, 2021



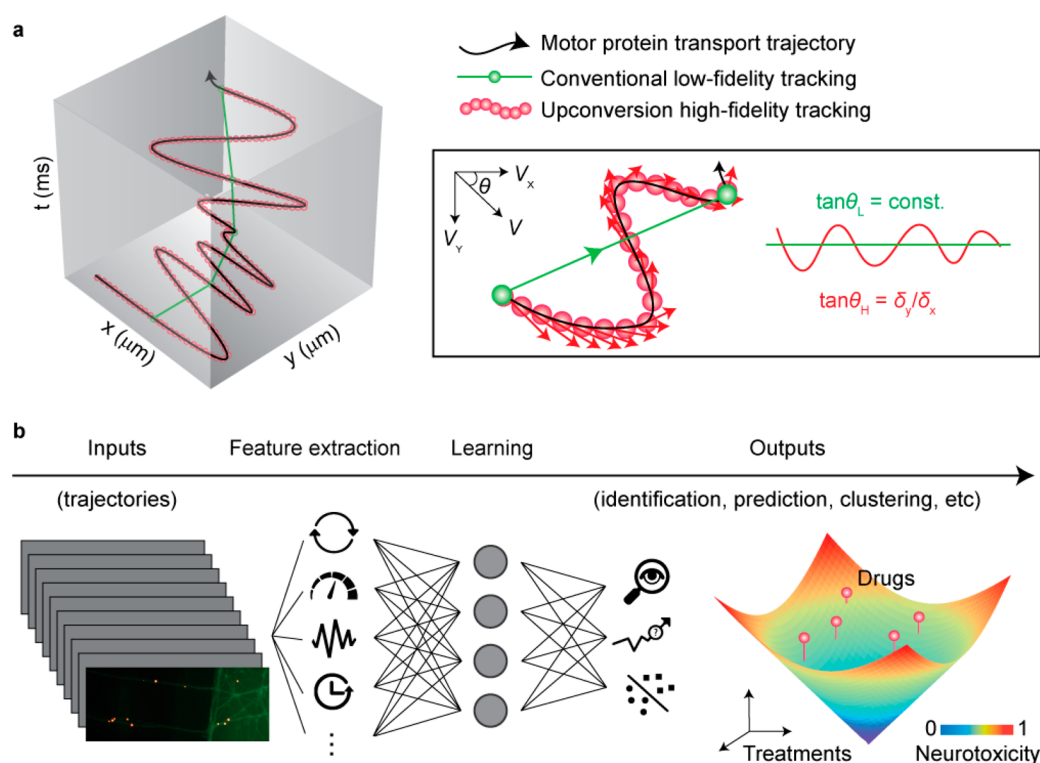


Figure 1. Schematic showing CIPN assessment based on upconversion high-fidelity intraneural tracking and machine learning. (a) Upconversion dynamic tracing with a high refreshment rate maintains high-fidelity trajectories of intraneural motor protein transport, in contrast to the relatively low fidelity achieved by conventional tracking methods using fluorescent dyes, proteins, quantum dots, or upconversion nanoparticles. The high fidelity benefits from the polynomial fitting of high frame-refreshing upconversion dynamic tracking with tunable instantaneous velocity. (b) Machine-learning model for the prediction and quantification of neurotoxicity, where the inputs are trajectories from upconversion microscopic records. The features include processivity, velocity, frequency, and duration of retro, antero, and pausing segments from vesicular movements. A mega-multidimensional library of drug-induced neuropathy can be established where the neurotoxicity is determined on the basis of multiple parameters such as drugs, cell type, dosage, and administrative time.

upconversion high-fidelity tracking and machine learning of intraneuronal transport.

RESULTS AND DISCUSSION

Upconversion Nanoprobe Design and Characterizations. To verify our hypothesis, we designed and synthesized upconversion nanoparticles with multilayer core-shell nanostructures and optimized the photoluminescent output. We determined that sodium fluoride based $\text{NaYbF}_4\text{:Tm}$ (2%) nanoparticles emit in the range of 400–850 nm (Figure S1). Further confinement of the $\text{Yb}^{3+}/\text{Tm}^{3+}$ couple into a sandwiched layer, formulated as $\text{NaYbF}_4\text{:Tm@NaYbF}_4$, enhanced energy transfer from Yb^{3+} to Tm^{3+} (Figure S2). The NaYF_4 shell layer was employed to suppress surface luminescence quenching. These rod-shaped nanocrystals have an average size of 33×68 nm. Their upconversion emission is over 10 times brighter than that of their $\text{NaYbF}_4\text{:Tm}$ counterpart and over 200 times brighter than that of conventional $\text{NaYF}_4\text{:Yb/Tm}$ nanocrystals. The photoluminescence enhancement is also confirmed by single-nanoparticle imaging, which is in accord with spectral data recorded in solution (Figure S3). These core-shell nanorods are ideal for implementing real-time tracking of intraneuronal transport at single-particle levels with high refreshment rates. We further coated these nanorods with a thin layer of silica to improve the hydrophilicity and biocompatibility (Figure S4). These silica-capped nanorods with a hydrodynamic size of ~ 90

nm in PBS buffer and neurobasal medium maintained long-term stability beyond 3 months.

High-Fidelity Upconversion Intraneural Tracking. We then utilized an *in vitro* integrated, two-compartment chamber to culture dorsal root ganglion (DRG) cells, one type of primary sensory neurons associated with neuropathic pain in the peripheral nervous system (Figure S5). Soma and axonal terminals were separated from one another by microtunnels. Nanoprobes supplemented in neurobasal medium were added to the axonal compartment and internalized into neuronal cells, followed by retrograde transport to the soma compartment. After incubation for 1 h, numerous nanoprobe cargoes were detected in axons and somas (Figure 2a–e and Movie S1). A statistical analysis of all emissive spots revealed that $\sim 99\%$ of the nanoprobes underwent retrograde transport (axon to soma) and approximately 1% of them returned to the axonal compartment via anterograde transport (soma to axon). Both pathways are common to intraneuronal transport.^{18,19} An example of retrograde and anterograde transport was illustrated, following the trajectories of bright spots (marked as 3 and 4 in Figure S6). The luminescent signal to noise ratio in neurons is over 15 when the exposure time of each frame is set at 50 ms, and the ratio remains over 3 with a 1 ms exposure time. Notably, no photoblinking or photobleaching was observed for nanoprobes in DRG neurons during the entire tracking period. The sub-micrometer spatial resolution in intraneuronal tracking revealed the trajectories of two bright spots (marked as 1 and 2) along the same axonal bundle, but

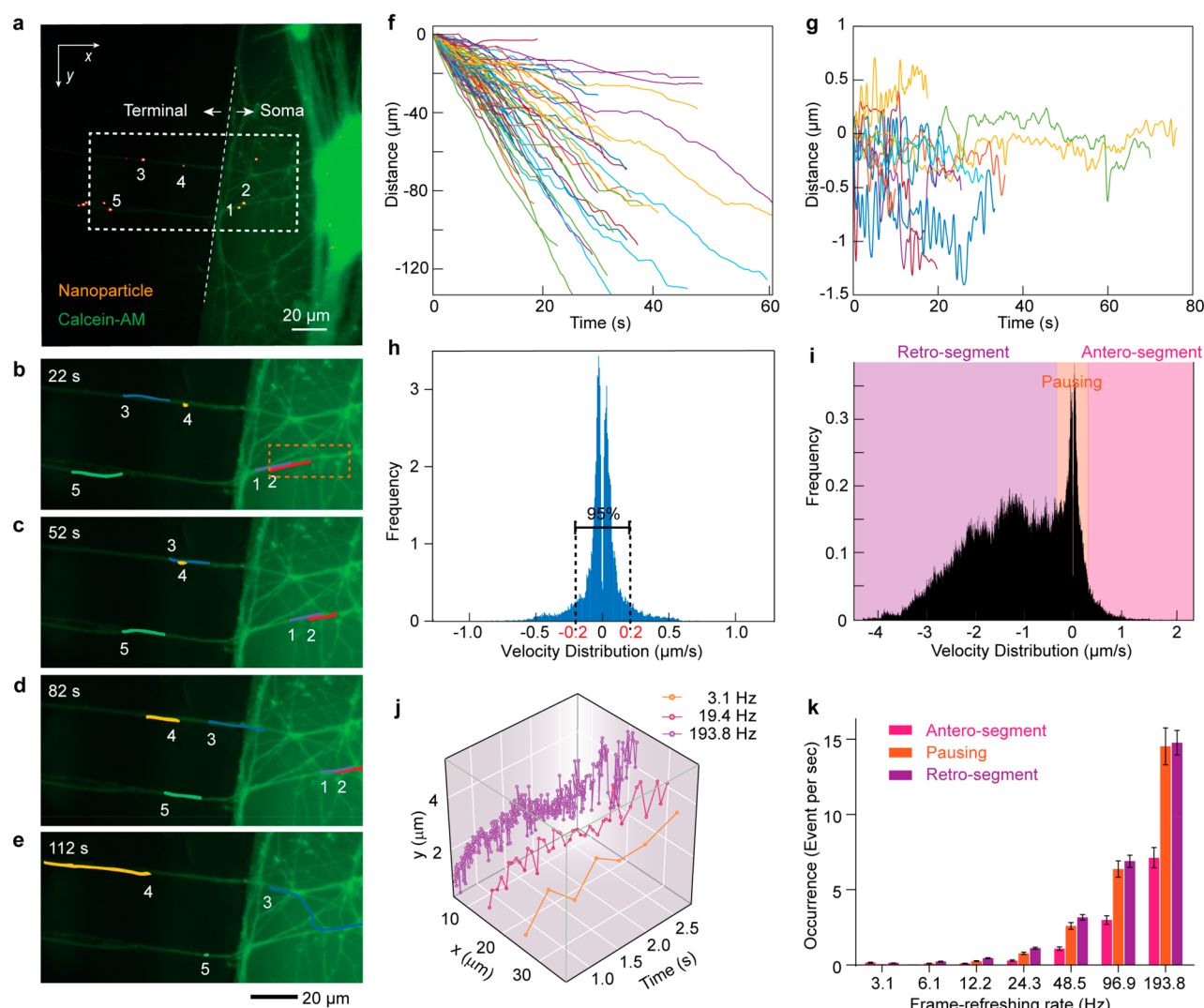


Figure 2. Real-time intraneuronal transport tracking in DRG neurons using upconversion nanoparticles. (a) Merged photoluminescence image showing colocalization between upconversion nanoprobe (yellow) and neural structures (green). (b–e) Time-lapse luminescence images of the white-dotted rectangular region in (a), showing five trajectories of cargo trafficking in neurons (exposure time, 5 ms; refresh frame frequency, 38 Hz). (f) Trajectories of nanoparticle-tethered cargoes in healthy DRG neurons (exposure time, 5 ms; refresh frame frequency, 193.8 Hz). (g) Trajectories and (h) velocity distribution of 10 nanoparticle-tethered cargoes collected from freshly fixed neurons ($n = 3$). Pausing-phase thresholds of intraneuronal transport are identified as $\pm 0.2 \mu\text{m/s}$ within a 95% confidence interval. (i) Velocity distribution profile of nanoparticle-tethered cargoes in (f). The profile is divided into retro/pausing/antero segments, depending on the determined velocity threshold. (j) Plotted trajectory profiles of one particle and (k) occurrence of retro/pausing/antero segments of all trajectories at different frame-refreshment rates, illustrating that a high fidelity of intraneuronal transport can only be achieved by high frame-refreshment rates in real-time tracking. Scale bars are expressed as means \pm SEM. Data in (f), (i), and (k) were collected from 80 emissive spots in healthy DRG neurons with 24 h post-treatment in 0.1 vol % DMSO in 26 video recordings where the cells were extracted from 6 individual batches of embryos.

via different axons. To investigate the pathways of nanoparticle internalization, we labeled lysosomes with LysoTracker in nanoprobe-pretreated DRG neurons and observed $\sim 7\%$ colocalization of nanoparticles with lysosomes (Figure S7). We also immunostained nanoparticle-containing cargoes and endosomes in fixed neurons, where markers EEA1/Rab5, Rab11, Rab7, and TGN38 correspond to early, late, recycling, and post-Golgi endosomes, respectively. The locations of $\sim 60\%$ of emitting spots matched those of endosomes, indicating that most of the nanoprobe had been taken into cells through endosomal pathways.^{18–20}

With the retrograde movement trend for nanoprobe-containing cargoes, “Stop and Go” phases of movable trajectories were observed (Figure 2f and Movie S2). We statistically analyzed trajectories from recorded videos and

quantified the transport parameters of nanoparticle-embedded endosomes. We define the “Stop” phase with a threshold below a velocity of $0.2 \mu\text{m/s}$ (95% confidence interval) in fixed neurons (Figure 2g,h). The dynamic variation in intraneuronal cargo transport was quantitatively evaluated according to specific “Stop and Go” features (Figure 2i). We quantified “Stop” (pausing) and “Go” (retrograde and anterograde) phases with four physical parameters: run length (in μm), processivity (in s), frequency (in events/min), and velocity (in $\mu\text{m/s}$). The velocity was determined by measuring the length of the displacement vector (run length) over time from the first to the last point (processivity) of each segment. A faster refreshment rate of frames reveals more details in intraneuronal transport (Figure 2j). To be exact, the occurrence of pausing and antero segments is likely to be

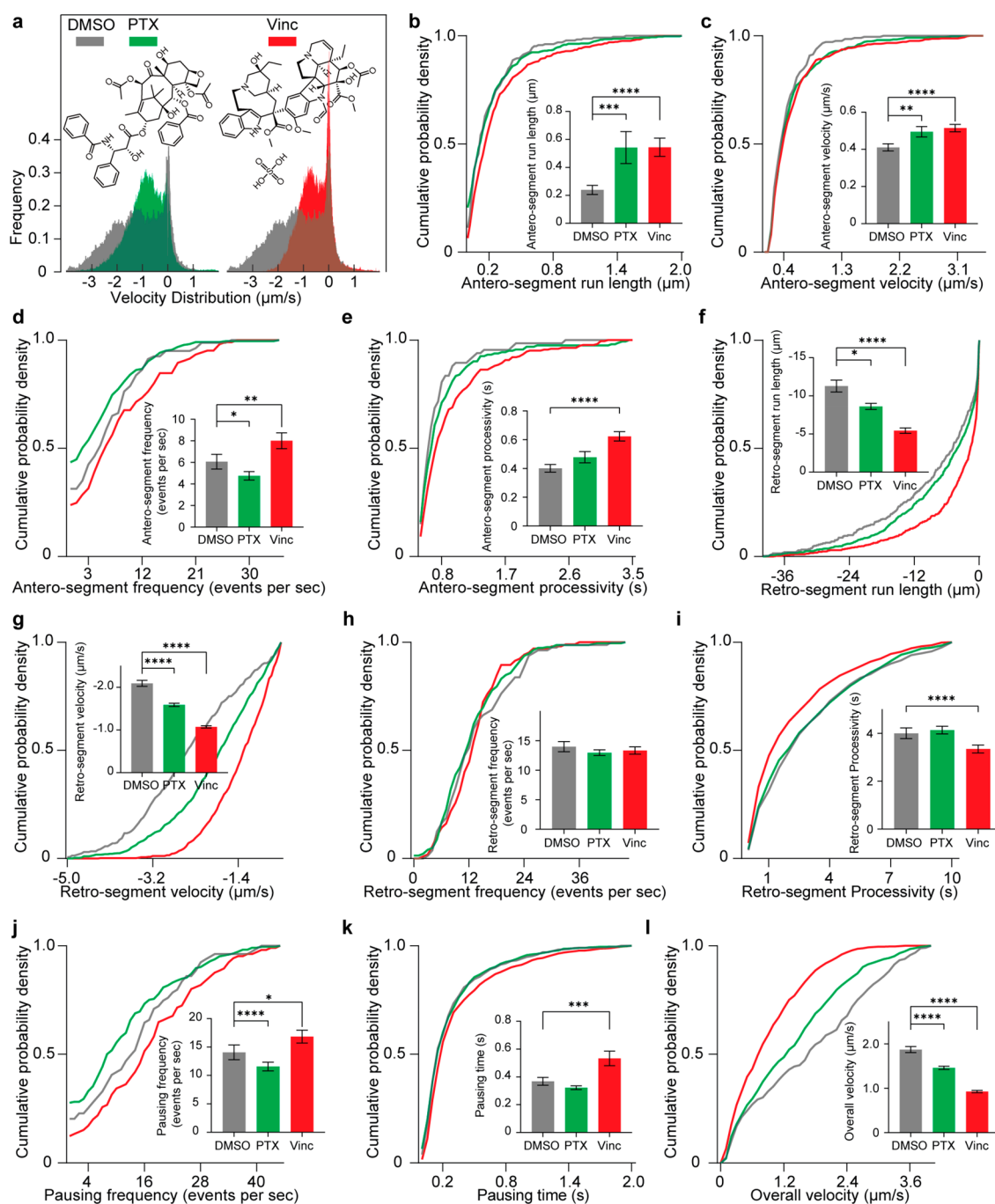


Figure 3. Effects of microtubule-active agents on intraneuronal transport. (a) Velocity distribution profiles of nanoparticles in each frame of the captured movies (see [Movies 2–4](#) in the Supporting Information). Insets: molecular structures of paclitaxel (PTX) and vincristine sulfate (Vinc). (b–l) Quantified physical parameters of intraneuronal transport in antero- and retrograde segments in terms of run length, velocity, frequency, and processivity. The quantitative analysis was based on numbers of individual trajectories/movies in each experimental group (80/26 for DMSO, 225/46 for PTX, and 105/37 for Vinc), where DRG cells were extracted from six batches of E15 embryos. The nanoprobe dosage was set as 100 nM for PTX and 10 nM for Vinc in 100 μ L of neuronal culture media. Data are presented as cumulative probabilities, and scale bars are expressed as means \pm SEM in inset plots. The statistical significance was assessed using the Kruskal–Wallis test with Dunn’s correction and the Wilcoxon test. Significance levels are stated as * $p < 0.05$, ** $p < 0.01$, *** $p < 0.001$, and **** $p < 0.0001$.

omitted at low refreshment rates ([Figure 2k](#)), resulting in insignificance of the corresponding run length, processivity, and velocity quantification. To achieve precise trajectory tracking and accurate quantitation of moving cargoes, we set the exposure time at 5 ms and lowered the capture window below 120 pixels in the longitudinal direction in an attempt to minimize the readout time of the camera. This led to a high temporal resolution of 193.8 Hz in video recording ([Movie](#)

[S2](#)). Unlike our previously reported low-frequency imaging (7 Hz),²¹ this high-frequency imaging (~ 200 Hz) mode can identify early signs of drug-induced neuropathy prior to collecting phenotype information.

Identification of Drug-Induced Abnormalities in Intraneuronal Movement. To verify the potential of the upconversion-based method for mapping drug-induced neuropathy, we tested two antineoplastic drugs, paclitaxel (PTX)

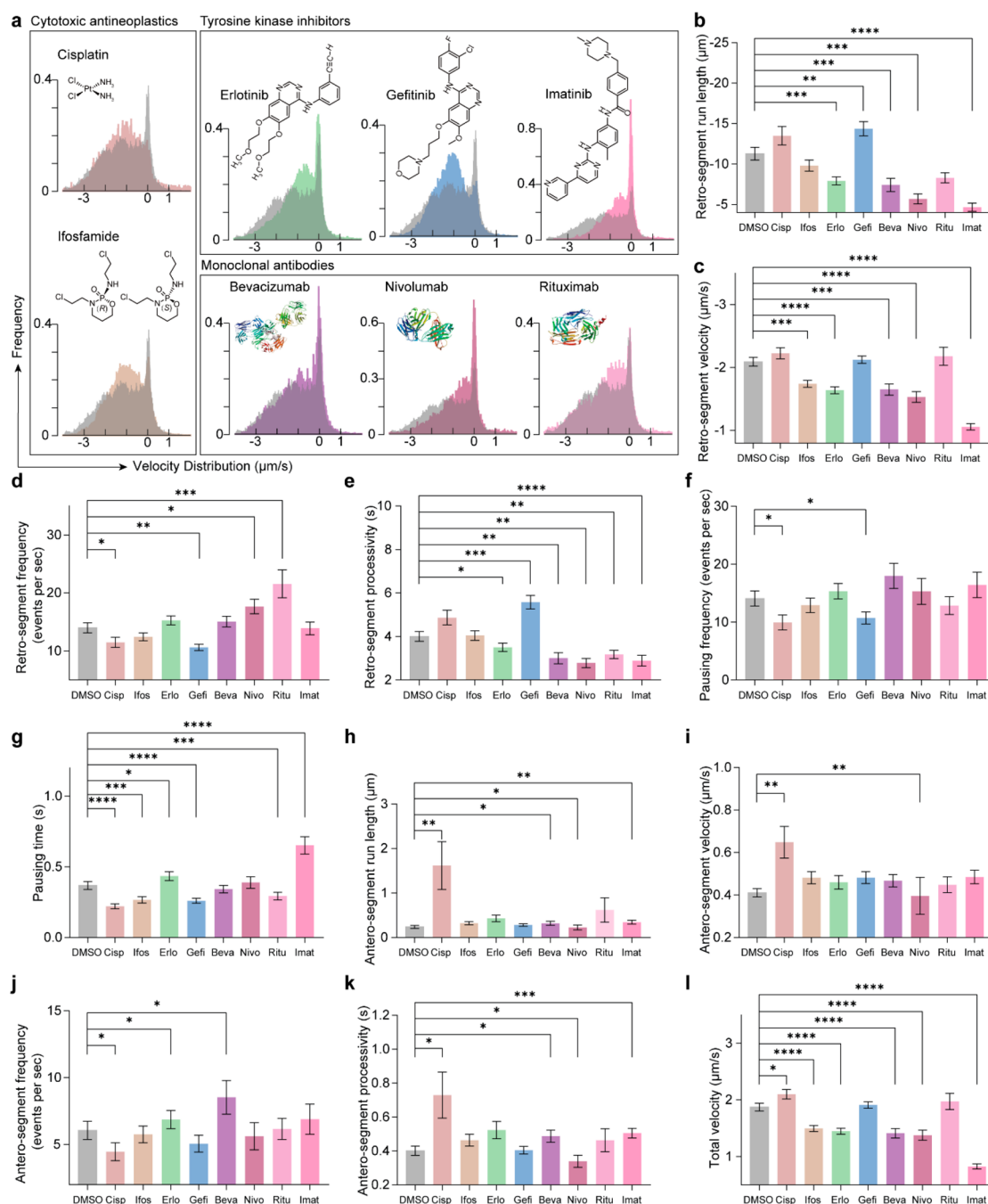


Figure 4. Expanding the upconversion microscopy technique for a universal drug-induced neuropathy assessment. (a) Velocity distribution profiles of moving nanoparticles collected from all frames of each movie. Insets are chemical or protein structures. (b–l) Quantified physical parameters of intraneuronal transport in antero- and retrograde segments in terms of run length, velocity, frequency, and processivity. The quantitative analysis was based on the numbers of independent trajectories/movies in individual groups (80/26 for DMSO, 78/14 for Cisp, 95/23 for Ifos, 109/26 for Erlo, 89/19 for Gefi, 69/8 for Beva, 96/11 for Nivo, 91/20 for Ritu, and 76/11 for Imat), where DRG cells were extracted from six batches of E15 embryos. The dosage was set as 100 nM for all drugs in 100 μ L of neuronal culture media. Scale bars in (b–l) represent means \pm SEM. Statistical significance was assessed using the Kruskal–Wallis test with Dunn’s correction and the Wilcoxon test. Significance levels are stated as * p < 0.05, ** p < 0.01, *** p < 0.001, and **** p < 0.0001.

and vincristine sulfate (Vinc), which are known to affect microtubule function during cellular proliferation (Figure 3a and Movies S3 and S4).^{5,6} Relative to the control group, PTX- and Vinc-treated groups showed decreased retrograde segmental velocities. However, Vinc binds directly to tubulin dimers and blocks their association to form microtubules, while PTX changes and stabilizes microtubule conformation to prevent its dissociation upon adenosine triphosphate (ATP)

hydrolysis.^{33,34} Further statistical and cumulative analyses revealed the similarity and distinction in the motion parameters of intraneuronal transport for both drug treatments (Figure 3b–l). It is likely that Vinc treatment decreases the cytoskeletal length and reduces the movement distance of motor proteins, leading to a relative increase in the number of attempts to interrupt antero-segment frequency and pausing frequency (Figure 3d,j). In contrast, PTX maintains the

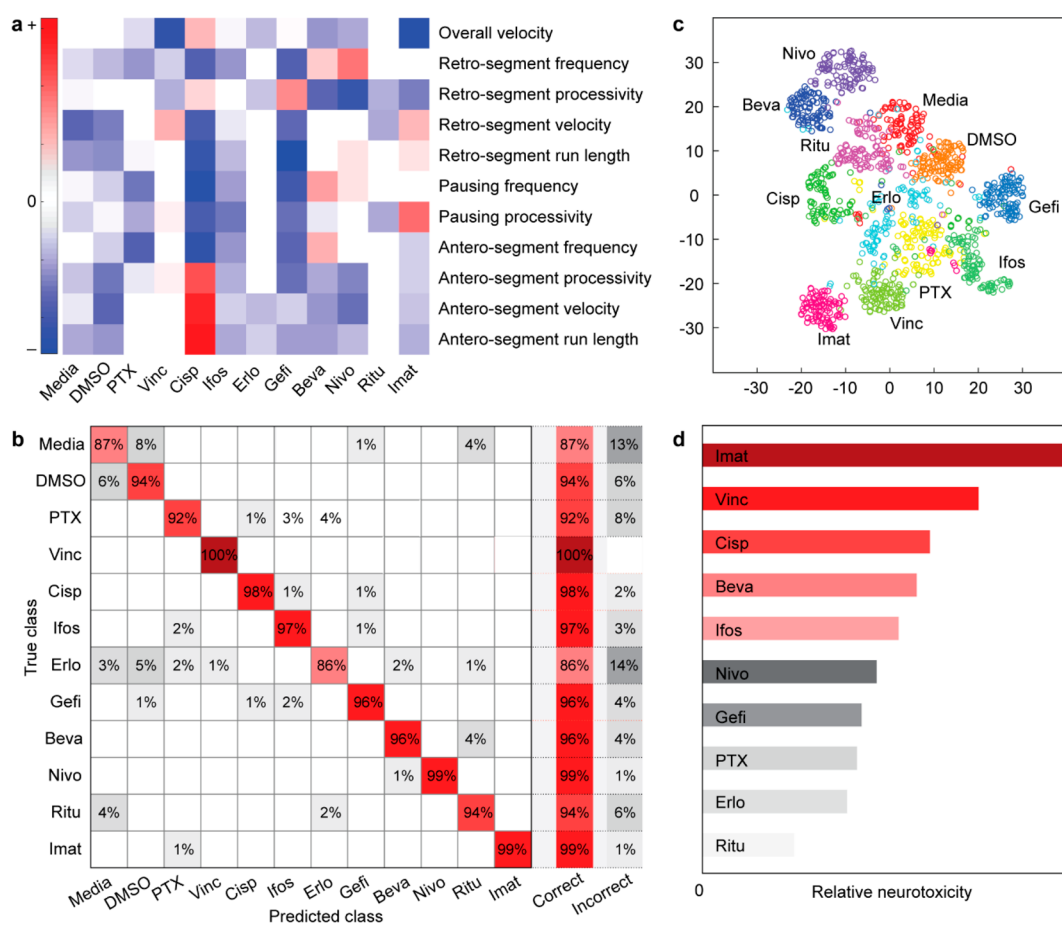


Figure 5. Machine learning validates the upconversion-based method for drug-induced neuropathy assessment. (a) Heat map showing averaged feature patterns of intraneuronal moving trajectories from all 12 tested groups. (b) Confusion matrix with prediction accuracy for the trained classifier using the support vector machine (SVM) algorithm. (c) Two-dimensional patterns showing the spatial relationship of drugs through *t*-distributed stochastic neighbor embedding (*t*-sne) as an approach to dimensional reduction. (d) Neurotoxicity rating of groups treated with a specific concentration of drugs on the basis of their moving trajectories.

stability of existing microtubule structures and prevents premature termination and attempts for motor protein transport, presenting a lower pausing frequency and antero-segment frequency. The possible effects of dimethyl sulfoxide (DMSO, 0.1 vol %) on cargo transport were excluded by quantifying all transport parameters (Figure S8).

We next investigated the possible changes induced by PTX and Vinc in DRG neurons at various levels, including growth morphology, gene expression, and neuronal functions. For instance, 24 h after pretreatment of DRGs with the two drugs, *in situ* microscopy imaging showed no marked changes in the sizes of somas and axons or in the neuronal morphology (Figure S9). The quantitative polymerase chain reaction (qPCR) revealed no significant differences in expression of microtubule-related genes ($p > 0.05$, Kruskal–Wallis test with Dunn’s correction and the Wilcoxon test) (Figure S10). In addition, an electrophysiological assessment indicated that PTX and Vinc did not affect the general neuronal function of DRG cells (Figure S11). The action potential threshold and latency were not markedly affected, although the frequency was slightly higher in neurons treated with PTX (Mann–Whitney *U* test, $p = 0.0446$) than in the control group. Further characterizations of the amplitude, half-width, hyperpolarization, and refractory period did not reveal any noticeable effect on action potential waveform in DRG neurons. When these

data are taken together, such short-term drug treatments induce no detectable phenotypes such as neuronal dysfunction or gene expression changes. Subtle changes in neuronal behaviors, which are undetectable using common biological or molecular approaches such as microscopic monitoring, qPCR, and electrophysiology, however, can be readily differentiated by our high-resolution upconversion microscopy.

We further examined the suitability of upconversion-mediated intraneuronal transport tracking for the neurotoxicity evaluation of various anticancer drugs, including cytotoxic antineoplastics (Cisp and Ifos), tyrosine kinase inhibitors (Erlo, Gefi, and Imat), and monoclonal antibodies (Beva, Nivo, and Ritu). Velocity distributions and motion parameters were drastically different among various drug treatments (Figure 4). Common features in velocity distribution showed that, for most drug treatments, the retrograde segmental frequency was reduced in high-speed regions ($< -2 \mu\text{m/s}$) but was increased in low-speed (-0.2 to $-2 \mu\text{m/s}$) and pausing (-0.2 to $0.2 \mu\text{m/s}$) regions (Figure 4a). These characteristics were also confirmed by a statistical analysis of classified parameters (Figure 4b–l). Although the drugs Gefi and Ritu induced no significant difference in nanoprobe velocity (Figure 4l), other motion characteristics such as pausing time and retrograde segmental processivity can be used to quantify how they differ from the control group.

In general, the mechanism of action underlying peripheral neuropathy induced by various antineoplastic drugs remains unclear. For example, cytotoxic antineoplastics affect the proliferation of cells by alkylating the guanine base of DNA molecules, thus preventing DNA elongation during replication.³⁵ As neurons are terminally differentiated and non-replicating, they are unlikely affected by the direct cytotoxic effect of Cisp and Ifos. Cisp has been shown to interact with non-DNA targets (phospholipids and proteins) and affect key neuron functional processes that are heavily dependent on protein and lipid raft interactions. For tyrosine kinase inhibitors, Gefi and Erlo are inhibitors of epidermal growth factor receptor (EGFR), while Imat is an inhibitor of several tyrosine kinase enzymes that regulate at least a few singling pathways.^{36,37} In our case, Gefi/Erlo and Imat have distinct effects in many parameters, although they are all tyrosine kinase inhibitors. Imat treatment possibly affects ATP hydrolysis and prevents the mechanical motion of motor proteins in a nonspecific manner, halting intraneural transport and shortening the run length (Figure 4b,g,h). Erlo and Gefi prevent EGFR autophosphorylation and the activation of downstream signaling pathways. However, it is not clear how EGF binding and EGFR activation affect whole-cell microtubule homeostasis. Monoclonal antibodies (Beva, Nivo, and Ritu) are specific targets of antitumor immune responses or vascular endothelial growth factor dependent vascularization, which may weakly affect neurons.

Machine Learning for Drug-Induced Neuropathy Assessment. We next applied machine learning to better understand intraneural transport and establish a comprehensive assessment system for CIPN. The integration of 11 motion features was used to develop machine-learning algorithms in the support vector machine (SVM) model. Feature characteristics under different drug conditions were preliminarily visualized by a parallel plot, whereas the upper and lower limits of the distribution were calculated according to means and standard deviations (Figure S12). Intra- and intergroup similarities between different drugs were determined by the average Euclidean distance of the 11-feature vector in each group or in various group pairs. Two-dimensional patterns demonstrate the spatial relationships of drugs using *t*-distributed stochastic neighbor embedding (*t*-sne) for dimensional reduction. The spatial proximity of patterns under different drug conditions indicates pharmaceutical similarity. On the basis of the preliminary analysis described above, feature fingerprints were generated through *z*-score normalization of the 11-feature matrix (Figure 5a). The fingerprint of control groups (DMSO and Media) displayed a light gray distribution with all values being near zero, serving as a baseline in comparison to other groups. The depth of blue and red lumps in other groups reveals pharmaceutical effects in several respects. The 11-feature matrix was employed for drug identification, in which a 94.8% accuracy was obtained (Figure 5b). The overall difference in drug treatments was visualized through clustering the 11 features in a separated spatial distribution (Figure 5c). We estimated toxicity scores by ranking the similarities between different drugs against the controls (Figure 5d). Among all tested groups, DMSO, Ritu, and Erlo exhibited low toxicity scores. The three monoclonal antibodies (Nivo, Beva, and Ritu) and two microtubule-active agents (PTX and Vinc) showed spatial proximity in the two-dimensional *t*-sne pattern, uncovering certain similarities in their internal categories. Of note, Gefi and Imat exhibited a

large spatial distance, despite both being tyrosine kinase inhibitors. Further systematic studies on various drugs, dosages, and treatment durations will facilitate the construction of a multidimensional database for CIPN assessment through machine learning as well as a deeper understanding of the underlying mechanisms.

CONCLUSIONS

Upconversion nanoparticles that offer bright near-infrared emission, high photostability, and superior biocompatibility are highly desirable for evaluating neuropathy models induced by chemical products. Subtle changes in neuropathy due to short-term drug treatment can be readily identified by upconversion-mediated, high-fidelity intraneuronal transport tracking. This approach offers unprecedented sensitivity for the early detection of drug-induced neuropathic disorders, unattainable with conventional biological approaches, before phenotype information becomes available. When this imaging platform is combined with machine learning, a comprehensive database of drug-induced neuropathy can be established, opening the door to the development of single-nanoparticle analysis tools for drug discovery, fundamental neuroscience, neuronal disorder diagnosis, and cancer therapeutics.

ASSOCIATED CONTENT

Supporting Information

The Supporting Information is available free of charge at <https://pubs.acs.org/doi/10.1021/jacs.1c07312>.

Materials and methods, detailed experimental procedures, algorithm for trajectory quantification, nanoparticle optimization and optical characterizations, single-particle imaging, stability, cellular uptake and growth, immunostaining, quantitative polymerase chain reaction, electrophysiology, and supplementary data for machine learning (PDF)

Videos from healthy DRGs, 38 Hz, from healthy DRGs, 193.8 Hz, from PTX-treated DRGs, 193.8 Hz, and from Vinc-treated DRGs, 193.8 Hz (ZIP)

AUTHOR INFORMATION

Corresponding Author

Xiaogang Liu – Department of Chemistry, National University of Singapore, Singapore 117543, Singapore; Center for Functional Materials, National University of Singapore Suzhou Research Institute, Suzhou 215123, People's Republic of China; The N1 Institute for Health, National University of Singapore, Singapore 117456, Singapore; Joint School of National University of Singapore and Tianjin University, International Campus of Tianjin University, Fuzhou 350207, People's Republic of China; Nanomedicine Translational Research Programme, Centre for NanoMedicine, Yong Loo Lin School of Medicine, National University of Singapore, Singapore 117609, Singapore; orcid.org/0000-0003-2517-5790; Email: chmlx@nus.edu.sg

Authors

Zhigao Yi – Department of Chemistry, National University of Singapore, Singapore 117543, Singapore; orcid.org/0000-0003-0853-2055

Huxin Gao – Center for Functional Materials, National University of Singapore Suzhou Research Institute, Suzhou 215123, People's Republic of China; Department of

Biomedical Engineering, National University of Singapore, Singapore 117583, Singapore

Xianglin Ji – Department of Biomedical Engineering, City University of Hong Kong, Kowloon, Hong Kong SAR 999077, People's Republic of China

Xin-Yi Yeo – Institute of Molecular and Cell Biology (IMCB), Agency for Science, Technology and Research (A*STAR), Singapore 138667, Singapore; Department of Physiology, Yong Loo Lin School of Medicine, National University of Singapore, Singapore 117593, Singapore

Suet Yen Chong – Department of Surgery, Yong Loo Lin School of Medicine, National University of Singapore, Singapore 119228, Singapore; Cardiovascular Research Institute (CVRI), National University Heart Centre Singapore (NUHCS), Singapore 117599, Singapore

Yujie Mao – Department of Chemistry, National University of Singapore, Singapore 117543, Singapore

Baiwen Luo – The N1 Institute for Health, National University of Singapore, Singapore 117456, Singapore

Chao Shen – College of Biology and Environmental Engineering, Zhejiang Shuren University, Hangzhou 310015, People's Republic of China

Sanyang Han – Department of Chemistry, National University of Singapore, Singapore 117543, Singapore

Jiong-Wei Wang – Department of Physiology, Yong Loo Lin School of Medicine, National University of Singapore, Singapore 117593, Singapore; Department of Surgery, Yong Loo Lin School of Medicine, National University of Singapore, Singapore 119228, Singapore; Cardiovascular Research Institute (CVRI), National University Heart Centre Singapore (NUHCS), Singapore 117599, Singapore; Nanomedicine Translational Research Programme, Centre for NanoMedicine, Yong Loo Lin School of Medicine, National University of Singapore, Singapore 117609, Singapore

Sangyong Jung – Institute of Molecular and Cell Biology (IMCB), Agency for Science, Technology and Research (A*STAR), Singapore 138667, Singapore; Department of Physiology, Yong Loo Lin School of Medicine, National University of Singapore, Singapore 117593, Singapore

Peng Shi – Department of Biomedical Engineering, City University of Hong Kong, Kowloon, Hong Kong SAR 999077, People's Republic of China; orcid.org/0000-0003-0629-4161

Hongliang Ren – Center for Functional Materials, National University of Singapore Suzhou Research Institute, Suzhou 215123, People's Republic of China; The N1 Institute for Health, National University of Singapore, Singapore 117456, Singapore; The Chinese University of Hong Kong (CUHK) Robotics Institute, Shatin, Hong Kong 999077, People's Republic of China

Complete contact information is available at:
<https://pubs.acs.org/10.1021/jacs.1c07312>

Notes

The authors declare no competing financial interest.

ACKNOWLEDGMENTS

This work was supported by the Agency for Science, Technology and Research (A*STAR) (A1983c0038), the National Research Foundation, Prime Minister's Office, Singapore, under the NRF Investigatorship program (Award No. NRF-NRFI05-2019-0003), the King Abdullah University

of Science and Technology (KAUST) Office of Sponsored Research (OSR) under Award No. OSR-2018-CRG7-3736, the NUS NANONASH Program (NUHSRO/2020/002/NanoNash/LOA; R143000B43114), the Singapore Ministry of Health's National Medical Research Council (NMRC/OFYIRG/0081/2018), and the National Natural Science Foundation of China (21771135, 21871071). S.Y.C. would like to thank the generous support from the ESR/TENG GL PhD scholarship program. We thank Akihiro Yamanaka, Angelo All, John Jia En Chua, Yinghua Qu, Liangliang Liang, Yuxia Liu, Sirui Liu, and Di Fu for helpful discussions.

REFERENCES

- (1) Stone, J. B.; DeAngelis, L. M. Cancer treatment-induced neurotoxicity: a focus on newer treatments. *Nat. Rev. Clin. Oncol.* **2016**, *13*, 92–105.
- (2) Magge, R. S.; DeAngelis, L. M. The double-edged sword: neurotoxicity of chemotherapy. *Blood Rev.* **2015**, *29*, 93–100.
- (3) Cavaletti, G.; Marmiroli, P. Chemotherapy-induced peripheral neurotoxicity. *Nat. Rev. Neurol.* **2010**, *6*, 657–666.
- (4) Lehmann, H. C.; Wunderlich, G.; Fink, G.; Sommer, R. C. Diagnosis of peripheral neuropathy. *Neurol. Res. Pract.* **2020**, *2*, 20.
- (5) Sisignano, M.; Baron, R.; Scholich, K.; Geisslinger, G. Mechanism-based treatment for chemotherapy-induced peripheral neuropathic pain. *Nat. Rev. Neurol.* **2014**, *10*, 694–707.
- (6) Zajączkowska, R.; Kocot-Kępska, M.; Leppert, W.; Wrzosek, A.; Mika, J.; Wordliczek, J. Mechanisms of chemotherapy-induced peripheral neuropathy. *Int. J. Mol. Sci.* **2019**, *20*, 1451.
- (7) Millicamps, S.; Julien, J. P. Axonal transport deficits and neurodegenerative diseases. *Nat. Rev. Neurosci.* **2013**, *14*, 161–176.
- (8) Sleight, J. N.; Rossor, A. M.; Fellows, A. D.; Tosolini, A. P.; Schiavo, G. Axonal transport and neurological disease. *Nat. Rev. Neurol.* **2019**, *15*, 691–703.
- (9) Stokin, G. B.; Lillo, C.; Falzone, T. L.; Brusch, R. G.; Rockenstein, E.; Mount, S. L.; Raman, R.; Davies, P.; Masliah, E.; Williams, D. S.; Goldstein, L. S. B. Axonopathy and transport deficits early in the pathogenesis of Alzheimer's disease. *Science* **2005**, *307*, 1282–1288.
- (10) Hirokawa, N. Kinesin and dynein superfamily proteins and the mechanism of organelle transport. *Science* **1998**, *279*, 519–526.
- (11) Vale, R. D. The molecular motor toolbox for intracellular transport. *Cell* **2003**, *112*, 467–480.
- (12) Roberts, A. J.; Kon, T.; Knight, P. J.; Sutoh, K.; Burgess, S. A. Functions and mechanics of dynein motor proteins. *Nat. Rev. Mol. Cell Biol.* **2013**, *14*, 713–726.
- (13) Qiu, W.; Derr, N. D.; Goodman, B. S.; Villa, E.; Wu, D.; Shih, W.; Reck-Peterson, S. L. Dynein achieves processive motion using both stochastic and coordinated stepping. *Nat. Struct. Mol. Biol.* **2012**, *19*, 193–200.
- (14) Hafezparast, M.; Klocke, R.; Ruhrberg, C.; Marquardt, A.; Ahmad-Annuar, A.; Bowen, S.; Lalli, G.; Witherden, A. S.; Hummerich, H.; Nicholson, S.; Morgan, P. J.; Oozageer, R.; Priestley, J. V.; Averill, S.; King, V. R.; Ball, S.; Peters, J.; Toda, T.; Yamamoto, A.; Hiraoka, Y.; Augustin, M.; Korthaus, D.; Wattler, S.; Wabnitz, P.; Dickneite, C.; Lampel, S.; Boehme, F.; Peraus, G.; Popp, A.; Rudelius, M.; Schlegel, J.; Fuchs, H.; de Angelis, M. H.; Schiavo, G.; Shima, D. T.; Russ, A. P.; Stumm, G.; Martin, J. E.; Fisher, E. M. C. Mutations in dynein link motor neuron degeneration to defects in retrograde transport. *Science* **2003**, *300*, 808–812.
- (15) Ross, J. L.; Wallace, K.; Shuman, H.; Goldman, Y. E.; Holzbaur, E. L. Processive bidirectional motion of dynein-dynactin complexes in vitro. *Nat. Cell Biol.* **2006**, *8*, 562–570.
- (16) McKenney, R. J.; Huynh, W.; Tanenbaum, M. E.; Bhabha, G.; Vale, R. D. Activation of cytoplasmic dynein motility by dynactin-cargo adapter complexes. *Science* **2014**, *345*, 337–341.
- (17) Pinaud, F.; Clarke, S.; Sittner, A.; Dahan, M. Probing cellular events, one quantum dot at a time. *Nat. Methods* **2010**, *7*, 275–285.

- (18) Cui, B.; Wu, C.; Chen, L.; Ramirez, A.; Bearer, E. L.; Li, W.; Mobley, W. C.; Chu, S. One at a time, live tracking of NGF axonal transport using quantum dots. *Proc. Natl. Acad. Sci. U. S. A.* **2007**, *104*, 13666–13671.
- (19) Haziza, S.; Mohan, N.; Loe-Mie, Y.; Lepagnol-Bestel, A.; Massou, S.; Adam, M.; Le, X. L.; Viard, J.; Plancon, C.; Daudin, R.; Koebel, P.; Dorard, E.; Rose, C.; Hsieh, F.; Wu, C.; Potier, B.; Herault, Y.; Sala, C.; Corvin, A.; Allinquant, B.; Chang, H.; Treussart, F.; Simonneau, M. Fluorescent nanodiamond tracking reveals intraneuronal transport abnormalities induced by brain-disease-related genetic risk factors. *Nat. Nanotechnol.* **2017**, *12*, 322–328.
- (20) Chowdary, P. D.; Che, D. L.; Kaplan, L.; Chen, O.; Pu, K.; Bawendi, M.; Cui, B. Nanoparticle-assisted optical tethering of endosomes reveals the cooperative function of dyneins in retrograde axonal transport. *Sci. Rep.* **2016**, *5*, 18059.
- (21) Zeng, X.; Chen, S.; Weitemier, A.; Han, S.; Blasiak, A.; Prasad, A.; Zheng, K.; Yi, Z.; Luo, B.; Yang, I.; Thakor, N.; Chai, C.; Lim, K.; McHugh, T. J.; All, A. H.; Liu, X. Visualization of intra-neuronal motor protein transport through upconversion microscopy. *Angew. Chem., Int. Ed.* **2019**, *58*, 9262–9268.
- (22) (a) Ou, X.; Qin, X.; Huang, B.; Zan, J.; Wu, Q.; Hong, Z.; Xie, L.; Bian, H.; Yi, Z.; Chen, X.; Wu, Y.; Song, X.; Li, J.; Chen, Q.; Yang, H.; Liu, X. High-resolution X-ray luminescence extension imaging. *Nature* **2021**, *590*, 410–415. (b) Han, S.; Deng, R.; Gu, Q.; Ni, L.; Huynh, U.; Zhang, J.; Yi, Z.; Zhao, B.; Tamura, H.; Pershin, A.; Xu, H.; Huang, Z.; Ahmad, S.; Abdi-Jalebi, M.; Sadhanala, A.; Tang, M.; Bakulin, A.; Beljonne, D.; Liu, X.; Rao, A. Lanthanide-doped inorganic nanoparticles turn molecular triplet excitons bright. *Nature* **2020**, *587*, 594–599.
- (23) Liu, Q.; Zhang, Y.; Peng, C. S.; Yang, T.; Joubert, L.; Chu, S. Single upconversion nanoparticle imaging at sub-10 W cm⁻² irradiance. *Nat. Photonics* **2018**, *12*, 548–553.
- (24) (a) Zhong, Y.; Ma, Z.; Wang, F.; Wang, X.; Yang, Y.; Liu, Y.; Zhao, X.; Li, J.; Du, H.; Zhang, M.; Cui, Q.; Zhu, S.; Sun, Q.; Wan, H.; Tian, Y.; Liu, Q.; Wang, W.; Garcia, K. C.; Dai, H. In vivo molecular imaging for immunotherapy using ultra-bright near-infrared-IIb rare-earth nanoparticles. *Nat. Biotechnol.* **2019**, *37*, 1322–1331. (b) Zhou, L.; Wang, R.; Yao, C.; Li, X.; Wang, C.; Zhang, X.; Xu, C.; Zeng, A.; Zhao, D.; Zhang, F. Single-band upconversion nanoprobes for multiplexed simultaneous in situ molecular mapping of cancer biomarkers. *Nat. Commun.* **2015**, *6*, 6938.
- (25) Nam, S. H.; Bae, Y. M.; Park, Y. I.; Kim, J. H.; Kim, H. M.; Choi, J. S.; Lee, K. T.; Hyeon, T.; Suh, Y. D. Long-term real-time tracking of lanthanide ion doped upconverting nanoparticles in living cells. *Angew. Chem.* **2011**, *123*, 6217–6221.
- (26) (a) Jiang, Y.; Fu, P.; Liu, Y.; Wang, C.; Zhao, P.; Chu, X.; Jiang, X.; Yang, W.; Wu, Y.; Wang, Y.; Xu, G.; Hu, J.; Bu, W. Near-infrared light-triggered NO release for spinal cord injury repair. *Sci. Adv.* **2020**, *6*, eabc3513. (b) Zhu, X.; Li, J.; Qiu, X.; Liu, Y.; Feng, W.; Li, F. Upconversion nanocomposite for programming combination cancer therapy by precise control of microscopic temperature. *Nat. Commun.* **2018**, *9*, 2176.
- (27) Wang, F.; Wen, S.; He, H.; Wang, B.; Zhou, Z.; Shimon, O.; Jin, D. Microscopic inspection and tracking of single upconversion nanoparticles in living cells. *Light: Sci. Appl.* **2018**, *7*, 18007.
- (28) Ma, Y.; Bao, J.; Zhang, Y.; Li, Z.; Zhou, X.; Wan, C.; Huang, L.; Zhao, Y.; Han, G.; Xue, T. Mammalian near-infrared image vision through injectable and self-powered retinal nanoantennae. *Cell* **2019**, *177*, 243–255.
- (29) Chen, S.; Weitemier, A. Z.; Zeng, X.; He, L.; Wang, X.; Tao, Y.; Huang, A. J. Y.; Hashimoto, Y.; Kano, M.; Iwasaki, H.; Parajuli, L. K.; Okabe, S.; Teh, D. B. L.; All, A. H.; Tsutsui-Kimura, I.; Tanaka, K. F.; Liu, X.; McHugh, T. J. Near-Infrared Deep Brain Stimulation Via Upconversion Nanoparticle-Mediated Optogenetics. *Science* **2018**, *359*, 679–684.
- (30) Butler, K. T.; Davies, D. W.; Cartwright, H.; Isayev, O.; Walsh, A. Machine learning for molecular and materials science. *Nature* **2018**, *559*, 547–555.
- (31) Feldmann, J.; Youngblood, N.; Wright, C. D.; Bhaskaran, H.; Pernice, W. H. P. All-optical spiking neurosynaptic networks with self-learning capabilities. *Nature* **2019**, *569*, 208–214.
- (32) Shastri, B. J.; Tait, A. N.; de Lima, T. F.; Pernice, W. H. P.; Bhaskaran, H.; Wright, C. D.; Prucnal, P. R. Photonics for artificial intelligence and neuromorphic computing. *Nat. Photonics* **2021**, *15*, 102–114.
- (33) Moudi, M.; Go, R.; Yien, C. Y. S.; Nazre, M. Vinca alkaloids. *Int. J. Prev. Med.* **2013**, *4*, 1231–1235.
- (34) Xiao, H.; Verdier-Pinard, P.; Fernandez-Fuentes, N.; Burd, B.; Angeletti, R.; Fiser, A.; Horwitz, S. B.; Orr, G. A. Insights into the mechanism of microtubule stabilization by Taxol. *Proc. Natl. Acad. Sci. U. S. A.* **2006**, *103*, 10166–10173.
- (35) Ralhan, R.; Kaur, J. Alkylating agents and cancer therapy. *Expert Opin. Ther. Pat.* **2007**, *17*, 1061–1075.
- (36) Bronte, G.; Rolfo, C.; Giovannetti, E.; Cicero, G.; Pauwels, P.; Passiglia, F.; Castiglia, M.; Rizzo, S.; Vullo, F. L.; Fiorentino, E.; Van Meerbeeck, J. Are erlotinib and gefitinib interchangeable, opposite or complementary for non-small cell lung cancer treatment? Biological, pharmacological and clinical aspects. *Crit. Rev. Oncol. Hematol.* **2014**, *89*, 300–313.
- (37) Joensuu, H.; Dimitrijevic, S. Tyrosine kinase inhibitor imatinib (STIS71) as an anticancer agent for solid tumours. *Ann. Med.* **2001**, *33*, 451–455.